Monthly Notices
of the
ROYAL ASTRONOMICAL SOCIETY

MNRAS **457,** 525–537 (2016) doi:10.1093/mnras/stw026

SN 2014J at M82 – I. A middle-class Type Ia supernova by all spectroscopic metrics

L. Galbany,[1,2★] M. E. Moreno-Raya,[3] P. Ruiz-Lapuente,[4,5] J. I. González Hernández,[6,7] J. Méndez,[8] P. Vallely,[9] E. Baron,[9] I. Domínguez,[10] M. Hamuy,[2,1] A. R. López-Sánchez,[11,12] M. Mollá,[3] S. Catalán,[13] E. A. Cooke,[14] C. Fariña,[8] R. Génova-Santos,[6,7] R. Karjalainen,[8] H. Lietzen,[6,7] J. McCormac,[13] F. C. Riddick,[8] J. A. Rubiño-Martín,[6,7] I. Skillen,[8] V. Tudor[8] and O. Vaduvescu[8]

[1]*Millennium Institute of Astrophysics, Universidad de Chile, Chile*
[2]*Departamento de Astronomía, Universidad de Chile, Santiago, Chile*
[3]*Departamento de Investigación Básica, CIEMAT, Avda. Complutense 40, E-28040, Madrid, Spain*
[4]*Instituto de Física Fundamental, Consejo Superior de Investigaciones Científicas, c/. Serrano 121, E-28006, Madrid, Spain*
[5]*Institut de Ciències del Cosmos (UB-IEEC), c/. Martí i Franqués 1, E-08028, Barcelona, Spain*
[6]*Instituto de Astrofísica de Canarias, E-38200 La Laguna, Tenerife, Spain*
[7]*Departamento de Astrofísica, Universidad de La Laguna (ULL), E-38206 La Laguna, Tenerife, Spain*
[8]*Isaac Newton Group of Telescopes, Apto. 321, E-38700, Santa Cruz de la Palma, Canary Islands, Spain*
[9]*Homer L. Dodge Department of Physics and Astronomy, University of Oklahoma, 440 W. Brooks, Rm 100, Norman, OK 73019-2061, USA*
[10]*Universidad de Granada, E-18071, Granada, Spain*
[11]*Australian Astronomical Observatory, PO Box 915, North Ryde, NSW 1670, Australia*
[12]*Department of Physics and Astronomy, Macquarie University, NSW 2109, Australia*
[13]*Department of Physics, University of Warwick, Gibbet Hill Road, Coventry CV4 7AL, UK*
[14]*School of Physics and Astronomy, University of Nottingham, University Park, Nottingham NG7 2RD, UK.*

Accepted 2016 January 4. Received 2016 January 1; in original form 2015 October 22

ABSTRACT

We present the intensive spectroscopic follow up of the Type Ia supernova (SN Ia) 2014J in the starburst galaxy M82. Twenty-seven optical spectra have been acquired from 2014 January 22 to September 1 with the Isaac Newton and William Herschel Telescopes. After correcting the observations for the recession velocity of M82 and for Milky Way and host galaxy extinction, we measured expansion velocities from spectral line blueshifts and pseudo-equivalent width of the strongest features in the spectra, which gives an idea on how elements are distributed within the ejecta. We position SN 2014J in the Benetti, Branch et al. and Wang et al. diagrams. These diagrams are based on properties of the Si II features and provide dynamical and chemical information about the SN ejecta. The nearby SN 2011fe, which showed little evidence for reddening in its host galaxy, is shown as a reference for comparisons. SN 2014J is a border-line object between the Core-normal and Broad-line groups, which corresponds to an intermediate position between low-velocity gradient and high-velocity gradient objects. SN 2014J follows the $R(\mathrm{Si\,II})$–Δm_{15} correlation, which confirms its classification as a relatively normal SN Ia. Our description of the SN Ia in terms of the evolution of the pseudo-equivalent width of various ions as well as the position in the various diagrams put this specific SN Ia into the overall sample of SN Ia.

Key words: methods: data analysis – techniques: spectroscopic – supernovae: general – supernovae: individual: 2014J.

1 INTRODUCTION

Type Ia supernovae (SNe Ia) are close binary systems where one of the stars, a carbon–oxygen white dwarf (C+O WD), undergoes a thermonuclear runaway following the start of explosive burning at its centre (Hoyle & Fowler 1960). The physics of the explosion is

★E-mail: lluisgalbany@gmail.com

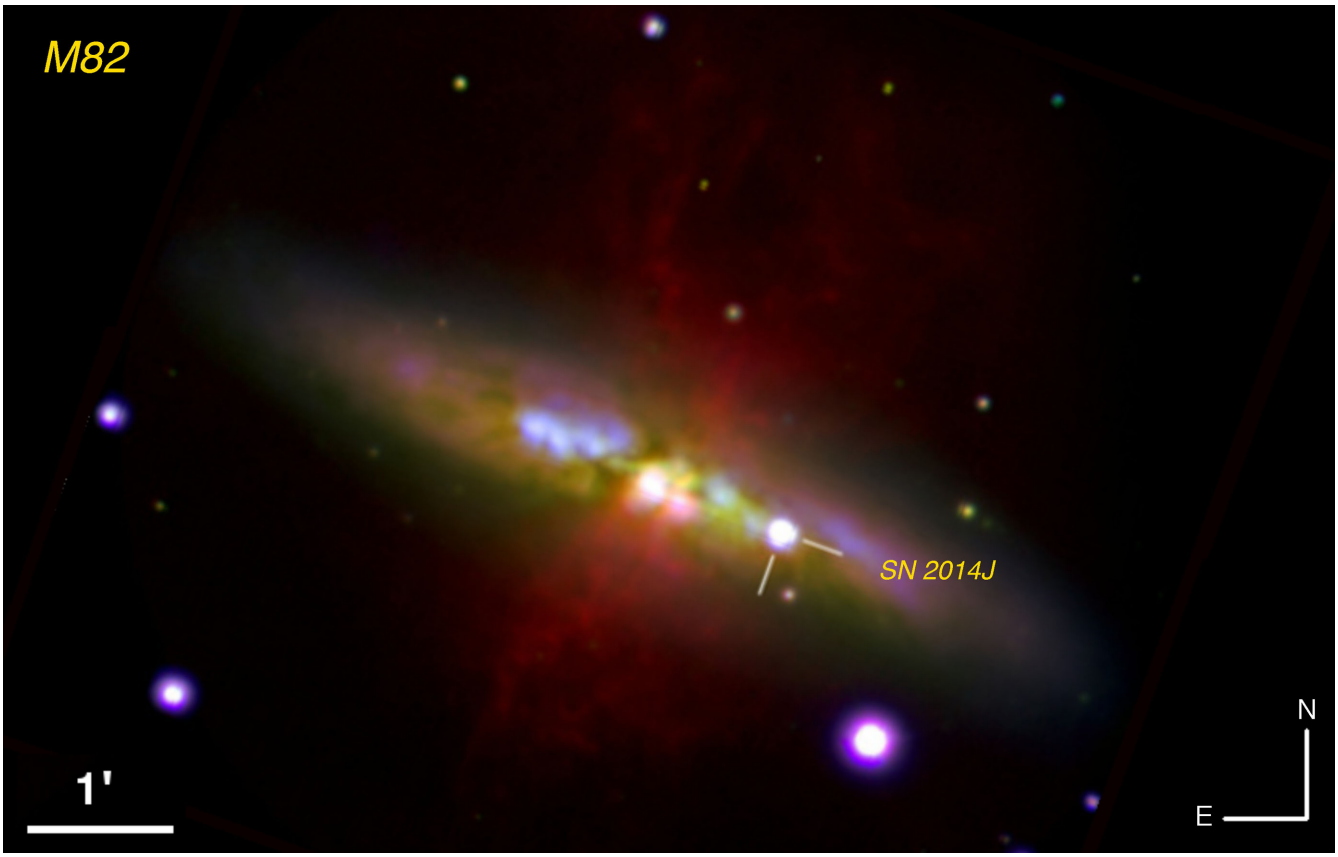

Figure 1. Type Ia SN 2014J in starburst galaxy M82. Image obtained using ACAM at 4.2 m William Herschel Telescope combining the following observations: 2 × 300 s in *u* (dark blue), 3 × 100 s in *g* (cyan), 3 × 200 s in *i* (green), 3 × 100 s in *r* (magenta), and 4 × 300 s in H α band filter (red).

determined by both components of the system. While the ejecta from the explosion (the supernova remnants, SNRs) have been studied in great detail, little is known yet about the companion star. It could be another WD (the DD channel; Iben & Tutukov 1984) or a star still fuelled by thermonuclear burning (the SD channel, Whelan & Iben 1973; it includes the case where the explosion is due to the merging of a WD with the core of an asymptotic giant branch star, proposed by Soker et al. 2013 and Livio & Riess 2003). See for recent reviews Hillebrandt et al. (2013), Maoz, Mannucci & Nelemans (2014), and Ruiz-Lapuente (2014).

A few SN Ia per century occur in a typical galaxy; hence, the probability of finding a nearby object is very low (Li et al. 2011). Therefore, the discovery of the nearby SN 2014J has become an excellent opportunity to improve the understanding on the supernova physics, by studying with in detail and with relatively high spatial resolution, the exploding star and its environment. In addition, precise characterization of their observed heterogeneity would be beneficial for reducing the systematic uncertainties of SN Ia distance method for cosmology.

SN 2014J exploded in the edge-on galaxy M82 (at $\alpha = 09^{h}55^{m}42.11^{s}$, $\delta = +69^{\circ}40'25.87$ arcsec, see Fig. 1) which is located only ∼3.5 Mpc away (Dalcanton et al. 2009). It is definitely the nearest SN Ia ever observed using modern instrumentation such as charge coupled devices (CCDs) (since SN 1987A was a peculiar Type II SN), surpassing SN 2011fe another SN Ia found in M101 ($d = 6.4 \pm 0.7$ Mpc). It rivals SN 1972E for being the closest SN Ia discovered in the last four decades, considering the large uncertainty in NGC 5253 distance estimation (SN 1972's host galaxy). SN 2014J was discovered serendipitously by Fossey et al. (2014) during a lesson on January 21.81 UT, while using the 0.35 m telescope at University of London Observatory. After Fossey reported the discovery, some pre-discovery observations were advertised (Denisenko et al. 2014; Ma et al. 2014).

SN 2014J was first classified as a SN Ia by Cao et al. (2014) from a spectrum obtained with the Dual Imaging Spectrograph on the Astrophysics Research Consortium (ARC) 3.5m telescope. As the nearest modern SN Ia, SN 2014J has been extremely well followed up by many groups, with different instruments, and in several wavelength ranges: γ-rays (Churazov et al. 2014; Diehl et al. 2014; Diehl 2015), X-rays (Margutti et al. 2014), UV (Brown et al. 2015), optical (Bonev et al. 2014; González-Hernández et al. 2014; Kotak 2014; Moreno-Raya et al. 2014; Poppe et al. 2015; Ritchey et al. 2015; Siverd et al. 2015), near-IR (Friesen et al. 2014; Goobar et al. 2014; Richardson et al. 2014; Marion et al. 2015; Vacca et al. 2015), mid-IR (Telesco et al. 2015), radio (Chandra et al. 2014; Chandler & Marvil 2014; Pérez-Torres et al. 2014; Sokolovsky et al. 2014; Chomiuk et al. 2015), and polarimetry (Kawabata et al. 2014; Patat et al. 2015).

A few weeks after the discovery the first analyses of this object were presented. The epoch of explosion was constrained to be around January 14.75 ± 0.30 UT (56671.75 MJD; Zheng et al. 2014; Goobar et al. 2015), and a maximum brightness in the *B* band of $M_B = -19.19 \pm 0.10$ mag, was reached on February 1.74 ± 0.13 UT (56689.74 MJD; Marion et al. 2015). Using optical photometry, Tsvetkov et al. (2014) estimated a decline rate parameter of $\Delta m_{15} = 1.01 \pm 0.05$ mag, while Ashall et al. (2014) reported 1.08 ± 0.03 mag, Marion et al. (2015) 1.12 ± 0.02 mag, and Kawabata et al. (2014) 1.02 ± 0.05 mag, pointing out that SN 2014J light curve has a typical stretch factor of a normal SN Ia. Due to the inclination with respect the line of sight of M82, SN 2014J has

shown to be highly affected by dust extinction. Amanullah et al. (2014) and Foley et al. (2014) presented extensive independent studies on extinction modelling, both arriving at the conclusion that an R_V (1.3 – 2.0) lower than the standard Galactic value (∼3.1) is needed to explain the observations, which is in agreement with the results from other work (Goobar et al. 2014; Brown et al. 2015; Gao et al. 2015), and confirmed with polarimetry by Kawabata et al. (2014) favouring dust grains with smaller radii and different nature than the typical Galactic dust. Radio and X-ray observations reported no detection of the SN in these wavelengths which was interpreted as a support for DD scenario for SN 2014J, and was also used to estimate the progenitor mass-loss rate (Margutti et al. 2014; Nielsen et al. 2014; Pérez-Torres et al. 2014). This estimate is in agreement with the upper limits estimated by Kelly et al. (2014) using *Hubble Space Telescope* data from near-UV to near-IR and by Lundqvist et al. (2015) using late optical spectra [but see Graham et al. 2015 for evidence of multiple components of circumstellar material (CSM) which would favour the SD scenario, and Kutsuna & Shigeyama (2015) who do not rule it out]. Interestingly, Crotts (2015) reported the discovery of light-echoes at ∼80 pc from the SN location revealing the CSM structure. Although all previous works have reported measurements of several properties that are in agreement with those of typical SN Ia, a proper spectral characterization and comparison to the whole SN Ia population has not been yet performed.

In the framework of a dedicated programme guaranteed by the Isaac Newton Group (ING), we obtained a long time baseline set of optical spectroscopy, with wavelengths from roughly 3500 Å to 9500 Å, with the 2.5m Isaac Newton (INT) and 4.2 m William Herschel (WHT) telescopes, both located at the El Roque de los Muchachos Observatory, La Palma. The spectral epochs range from almost two weeks pre-maximum (2014 January 22) to nearly seven months post-maximum (2014 September 1). A total of 27 different epochs were acquired with different instruments, technical configurations, and spectral resolutions. In addition, several broad-band images were also taken on different epochs. In Fig. 1, we show a false colour image of the SN 2014J and its host galaxy M82, composed from our observations at the WHT using *ugri* and H α filter images.

In this work, we present these observations (in Section 2), and describe the characterization of SN 2014J in the spectral SN Ia diagrams of Benetti et al. (2005, hereafter BE05), Branch et al. (2006, hereafter BR06) and Wang et al. (2009, hereafter WA09), together with the evolution of the velocity and pseudo-equivalent width (pW) of several spectral features (See Parrent, Friesen & Parthasarathy 2014 for an extended review on SN Ia spectroscopy). We also use SN 2011fe as a reference for comparisons. Those diagrams provide information on the dynamics and chemical distribution of SN Ia events, and have been of great utility to characterize large samples of SN Ia such as the CfA sample (Blondin et al. 2012) or the Carnegie Supernovae Project (CSP; Folatelli et al. 2013). We add this very well-studied SN Ia into the overall samples for a better understanding of this event (Sections 3 and 4). Finally, in Section 5, we give a summary and conclusions. A comparison with synthetic spectra using SYNOW (Branch et al. 2007) is presented in Paper II (Vallely et al. 2015).

2 OBSERVATIONS AND REDUCTION

We obtained long-slit spectroscopy of SN 2014J using the 2.5 m INT and 4.2 m WHT telescopes, both located at the El Roque de los Muchachos Observatory on La Palma. Spectra were obtained on 27 nights from 2014 January 22 to September 1 in different ways: observation time was allocated to the ING service proposal SW2014a08: Spectroscopic follow-up of SN 2014J, (PI: P. Ruiz-Lapuente), ING discretionary time on the INT, and time offered by several programmes both at WHT and INT. Since both the observers and the configuration of the instruments changed every night, we describe separately the different setups for each spectrograph. Details for individual spectra are given in Table 1.

2.1 Observations using 2.5 m INT

Four spectra (on nights January 22, February 03, 11 and 13) were obtained using the Intermediate Dispersion Spectrograph (IDS) mounted at the Cassegrain focus of the INT. Two detectors were used depending on the set up in different nights. On January 22, the EEV10 detector was used, which has a pixel size of 13.5 μm and a spatial dispersion of 0.40 arcsec pix^{-1}. The observation was performed with the R1200R grating, with a spectral dispersion of 0.47 Å pix^{-1}, and a 1 arcsec-width slit. On the other three nights, the REDPLUS2 detector, with a pixel size of 15 μm and a spatial dispersion of 0.44 arcsec pix^{-1}, was used. Observations were performed with three different gratings: R1200Y (spectral dispersion of 0.53 Å pix^{-1}) and the 1.3 arcsec slit; R300V (spectral dispersion of 2.06 Å pix^{-1}) with the 1.2 arcsec slit; and R400V (spectral dispersion of 1.55 Å pix^{-1}) with the 8 arcsec slit.

2.2 Observations using 4.2 m WHT

The remaining spectra were taken at the 4.2 m WHT using either the IDS and Imaging System (ISIS) or the Auxiliary-port CAMera (ACAM).

ISIS is mounted at the Cassegrain focus and consists of a dual-beam spectrograph with two independent arms which provide simultaneous observations in blue and red bands of the spectrum. The blue arm incorporates an EEV12 detector, with a pixel size of 13.5 μm, and spatial dispersion of 0.20 arcsec pix^{-1}. The gratings used were: R600B (spectral dispersion of 0.45 Å pix^{-1}), R300B (spectral dispersion of 0.86 Å pix^{-1}) and R158B (spectral dispersion of 1.62 Å pix^{-1}). Slit width was 1 arcsec in all cases. The red arm has a REDPLUS detector, with a pixel size of 15.0 μm and a spatial dispersion of 0.22 arcsec pix^{-1}. In this arm, the configurations used have the following specifications: R600R (spectral dispersion 0.49 Å pix^{-1}); R316R (spectral dispersion 0.93 Å pix^{-1}); and R158R (spectral dispersion 1.81 Å pix^{-1}). Slit width was also 1 arcsec in all cases.

ACAM is mounted permanently at a folded-Cassegrain focus, and it provides fixed-format low-resolution spectroscopy. All spectra were taken with the 400-line grism V400, which covers a spectral range from ∼ 3500 to ∼ 9400 Å (∼3.3 Å pix^{-1}), and it has a spatial dispersion of 0.25 arcsec pix^{-1}. Slit width was 1 arcsec for all cases except one (January 28) when the 2.0 arcsec wide slit was used.

2.3 Reduction

All spectra have been reduced using standard IRAF[1] routines, including debiasing and flat-fielding. The spectra have been calibrated in wavelength taking observations of internal arc lamps installed in

[1] Image Reduction Analysis Facility, distributed by the National Optical Astronomy Observatories (NOAO), which is operated by AURA Inc., under cooperative agreement with NSF.

Table 1. Instrument specifications for the observations presented in this work.

Date (UT)	Epoch (days)	Telescope	Instrument	Grism/ grating	Camera detector	Exp. time (s)	Spatial disp. (arcsec pix^{-1})	Spectral disp. (Å pix^{-1})	λ range (Å)	Slit width (arcsec)
JAN 23.18	−9.6	INT	IDS	R1200R	EEV10	4×300	0.40	0.47	5800–7400	1.0
JAN 24.23	−8.5	WHT	ACAM	V400	AUXCAM	3×60	0.25	3.30	3500–9400	1.0
JAN 25.30	−7.4	WHT	ACAM	V400	AUXCAM	2×200	0.25	3.30	3500–9400	1.0
		WHT	ISIS	R600B	EEV12	2×900	0.20	0.45	3526–5350	1.0
		WHT	ISIS	R600R	REDPLUS	2×900	0.22	0.49	4872–6926	1.0
		WHT	ISIS	R600R	REDPLUS	2×900	0.22	0.49	5757–7811	1.0
JAN 26.25	−6.5	WHT	ACAM	V400	AUXCAM	3×200	0.25	3.30	3500–9400	1.0
JAN 27.30	−5.4	WHT	ACAM	V400	AUXCAM	2×200	0.25	3.30	3500–9400	1.0
		WHT	ISIS	R1200B	EEV12	2×1200	0.20	0.45	3480–4420	1.0
		WHT	ISIS	R1200R	REDPLUS	3×600	0.22	0.49	5361–6416	1.0
JAN 28.11	−4.6	WHT	ACAM	V400	AUXCAM	2×15	0.25	3.30	3500–9400	2.0
FEB 04.05	+2.3	INT	IDS	R1200Y	REDPLUS2	3×120	0.44	0.53	4900–6400	1.3
		INT	IDS	R1200Y	REDPLUS2	3×90	0.44	0.53	5860–7400	1.3
FEB 05.06	+3.3	WHT	ISIS	R600B	EEV12	2×60	0.20	0.45	3700–5050	1.0
		WHT	ISIS	R600R	REDPLUS	2×60	0.22	0.49	5600–7150	1.0
FEB 05.93	+4.2	WHT	ISIS	R600B	EEV12	2×120	0.20	0.45	3650–5050	1.0
		WHT	ISIS	R600R	REDPLUS	2×20	0.22	0.49	5650–7200	1.0
FEB 12.27	+10.5	INT	IDS	R300V	REDPLUS2	7×60	0.44	2.06	4700–9900	1.2
FEB 14.10	+12.4	INT	IDS	R400V	REDPLUS2	6×120	0.44	1.55	4400–7400	8.0
FEB 19.18	+17.4	WHT	ACAM	V400	AUXCAM	3×30	0.25	3.30	4900–9300	1.0
FEB 20.07	+18.3	WHT	ACAM	V400	AUXCAM	3×30	0.25	3.30	4900–9300	1.0
FEB 21.20	+19.5	WHT	ACAM	V400	AUXCAM	3×30	0.25	3.30	4900–9300	1.0
FEB 24.19	+22.5	WHT	ACAM	V400	AUXCAM	7×30	0.25	3.30	4900–9300	1.0
FEB 26.27	+24.5	WHT	ACAM	V400	AUXCAM	1×30	0.25	3.30	4900–9300	1.0
MAR 07.18	+33.4	WHT	ACAM	V400	AUXCAM	2×30	0.25	3.30	4900–9300	1.0
MAR 08.16	+34.4	WHT	ACAM	V400	AUXCAM	1×30	0.25	3.30	4900–9300	1.0
MAR 12.86	+39.1	WHT	ACAM	V400	AUXCAM	1×30	0.25	3.30	4100–9200	1.0
MAR 18.14	+44.4	WHT	ACAM	V400	AUXCAM	1×30	0.25	3.30	4100–9200	1.0
APR 08.91	+66.2	WHT	ACAM	V400	AUXCAM	1×60	0.25	3.30	4900–9300	1.0
MAY 08.91	+96.2	WHT	ACAM	V400	AUXCAM	1×30	0.25	3.30	4900–9300	1.0
MAY 09.90	+97.2	WHT	ISIS	R300B	EEV12	3×60	0.20	0.86	3700–5350	1.0
		WHT	ISIS	R316R	REDPLUS	3×60	0.22	0.93	5350–8000	1.0
MAY 11.89	+99.1	WHT	ISIS	R600B	EEV12	3×30	0.20	0.45	3700–5350	1.0
		WHT	ISIS	R600R	REDPLUS	3×60	0.22	0.49	6200–7700	1.0
JUN 18.93	+137.2	WHT	ISIS	R158B	EEV12	1×300	0.20	1.62	3650–5050	1.0
		WHT	ISIS	R158R	REDPLUS	1×300	0.22	1.81	5500–9050	1.0
JUL 08.89	+157.2	WHT	ACAM	V400	AUXCAM	1×120	0.25	3.30	4900–9300	1.0
SEP 02.23	+212.5	WHT	ACAM	V400	AUXCAM	1×30	0.25	3.30	4900–9300	1.0

the Acquisition and Guiding Box using the same instrumental configuration as for the science observations. The following standard stars were observed for the flux calibration: HD 93521, BD08 2015, Grw+70 5824, G191−B2B, Feige 34, BD+75 325, PG0934+554 belonging to Massey et al. (1988), Oke (1990) and Stone (1977) catalogues; and HD 109995, all included in the standard data base of IRAF. The routines used for these purposes were: IDENTIFY, REIDENTIFY, FITCOORDS and TRANSFORM (for calibration in wavelength); and STANDARD, SENSFUNC and CALIBRATE (for flux calibration). In Fig. 2, we show examples of three 2D spectra from different instruments at both telescopes, where the wavelength coverage, strong emission lines, and sky contamination can be seen. Fig. 3 shows a composite of the fully reduced observed spectra, where all have been shifted to the rest frame by the recession velocity of M82 ($v = 203$ km s^{-1}). The complete set of spectroscopy is available electronically[2] or can be downloaded from the Weizmann interactive supernova data repository (WISeREP;[3] Yaron & Gal-Yam 2012).

3 SPECTRAL CHARACTERIZATION

The evolution of several spectral features is clearly seen in Fig. 3, including the typical features found in SN Ia spectra: Ca II H&K, Si II λ4130, Mg II, S II W, Si II λ5972, Si II λ6355, and Ca II triplet. There is also evidence of high-velocity features (e.g. HV Ca II at ∼7900 Å in the pre-maximum spectra). Telluric lines, marked with Earth symbols, and interstellar medium absorptions from the host galaxy, such as NaD λ5900, have not been removed in the figure but in the measurements when necessary. From bluer wavelengths we see, as pointed out by previous works, that the SN is heavily reddened by dust in the host galaxy. Although the spectra shown in the figure have not been corrected for Milky Way (MW) and host galaxy extinction,

[2] https://github.com/lgalbany/SN2014J

[3] http://wiserep.weizmann.ac.il

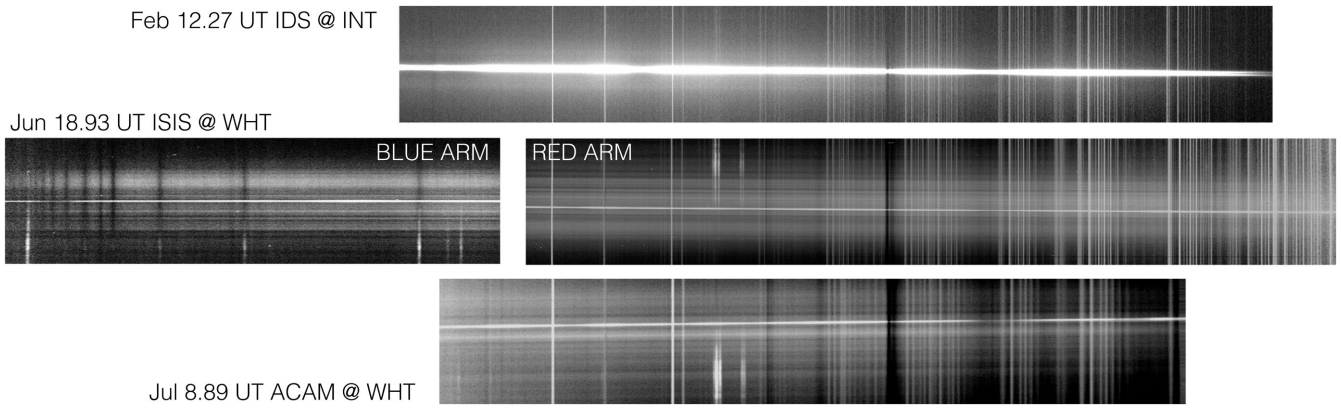

Figure 2. 2D spectra of SN 2014J taken with different instruments at both telescopes. Top row: spectrum taken at INT using IDS covering the spectral range of 4700–9900 Å with R300V. Mid-row: blue and red arm spectra taken with ISIS at WHT, taken with the R600B and R600R gratings, respectively. The wavelength coverage range from 3650 to 5050 Å in the blue arm and from 5500 to 9050 Å in the red arm. Bottom row: ACAM spectrum covering the optical range of 4900–9300 Å. Several emission lines from the host galaxy M82 can be seen in the mid- and bottom spectra.

the spectral parameters described below have been measured after applying these corrections using a Fitzpatrick 1999 law, for both the MW using the dust maps of Schlafly & Finkbeiner (2011) assuming an $R_V = 3.1$, and for the host galaxy with the reported values of $E(B-V) = 1.2$ and $R_V = 1.4$ from Goobar et al. (2014).

3.1 Measurement of the spectral parameters

For the most prominent features listed above, we measured their expansion velocity (v) and pW when the data allowed. The depth of the feature (d) has been also measured for the Si II λ5972 and Si II λ6355 absorptions (See Fig. 4 for a representation of these three parameters). Their measurement has been performed as follows. First, two adjacent continuum regions 15 Å wide around the feature were selected. These were used to perform a bootstrapping method using the 225 different combinations of two points, one from the blue and one from the red regions. For each repetition, a segment representing the pseudo-continuum was drawn and used to normalize the observed spectrum. In the normalized spectrum, a Gaussian fit was performed to determine the wavelength (λ_e) at which the minimum of the feature fell. For each of the 225 repetitions, we store λ_e, the depth d from the pseudo-continuum to the normalized spectrum at that wavelength, and the integral of the feature on the normalized spectrum (pW) from the pseudo-continuum. Moreover, we kept all individual uncertainties coming from the instrumental flux errors. Finally, we averaged the 225 measurements and uncertainties of λ_e, d, and pW, and used the standard deviation of their distributions as a systematic uncertainty, which has been added in quadrature to the instrumental error. Velocities are derived from the shift of the average minimum of the feature with respect the expected rest-frame wavelength, via the relativistic Doppler formula,

$$v = c\frac{[(\Delta\lambda/\lambda_0)+1]^2 - 1}{[(\Delta\lambda/\lambda_0)+1]^2 + 1}, \quad (1)$$

where λ_0 is the rest-frame wavelength of the corresponding feature, and $\Delta\lambda$ is the difference between the measured wavelength λ_e and λ_0. In Tables 2 and 3, we present the resulting measurements for v and pW, respectively.

The reddening modifies the shape of the spectrum reducing the flux more strongly in bluer wavelengths and producing an effect on spectral features. Although the minima of the spectral features is not going to be strongly affected (thus the v), both the slope of the pseudo-continuum and its deepness would be affected. Nordin et al. (2011) and Garavini et al. (2007) studied the effect of reddening in the uncertainties of pW measurement and concluded that for values of $E(B-V)$ lower than 0.3 the difference is lower than 5 per cent, but for more extinguished SN, it could be important, which is the case of SN 2014J. To avoid a systematic error from reddening, we deredden all spectra as described above before measuring line parameters.

3.2 Spectral diagnostic diagrams

Several spectral indicators have been used in the literature to study the properties of SN Ia and interpret their heterogeneities.

Nugent et al. (1995) defined the fractional depth of the Si II λ5972 through the Si II λ6355 absorptions in the near-maximum light spectrum, $R(\mathrm{Si\,II}) = \frac{d_{5972}}{d_{6355}}$, and showed that it correlates well with the absolute magnitude at peak, which in turn correlates with the brightness decline rate through the Phillips (1993) relation: the more luminous the SN Ia, the lower the R(Si II) at maximum light and the slower the brightness decline. Both photometric and spectroscopic heterogeneities are attributed to differences in the effective temperature, which depend on total amount of ^{56}Ni produced in the explosion and the kinetic energy. The former can be estimated from the brightness decay in the bolometric light curve, and the latter from the expansion velocity of the ejecta. However, the lack of correlation between the R(Si II) and the photospheric velocity (deduced from Si II λ6355 blueshift) pointed out that only one parameter cannot account for the SN Ia spectroscopic diversity (Hatano et al. 2000). In fact, the current widely spread SN Ia photometric standardization needs two parameters (stretch and colour; Guy et al. 2007; Jha, Riess & Kirshner 2007; Conley et al. 2008) to reduce the scatter on the peak magnitudes, and even a third parameter accounting for the environment has been proposed (Lampeitl et al. 2010; Sullivan et al. 2010; Betoule et al. 2014; Moreno-Raya et al. 2015).

BE05 studied the evolution of the R(Si II) ratio and proposed that SN Ia could be well separated in two groups depending on their value at maximum: (i) high-velocity gradient (HVG) SN Ia, with

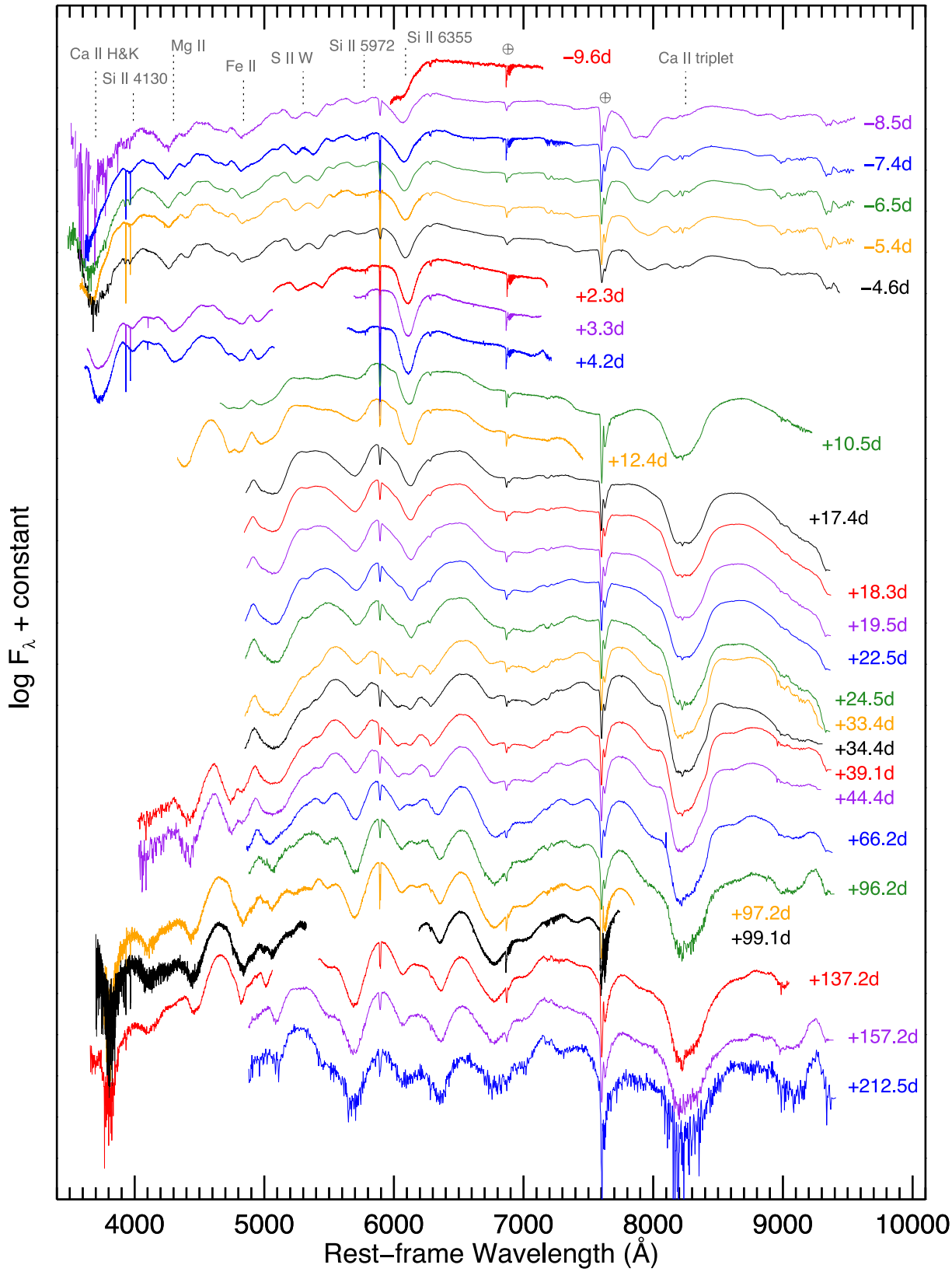

Figure 3. Spectral evolution of SN 2014J. Observed unredshifted pre-maximum, maximum-light, and post-maximum spectra taken at ORM (La Palma). The maximum light in the *B* band has been determined to be at February 1.74 ± 0.13 UT (56689.74 MJD). For epochs −7.4d and −5.4d from maximum, 3 and 2, respectively high-resolution spectra have also been observed, and here we show a composite of these and the low-res spectra.

Table 2. Measured velocities (in units of 10^3 km s^{-1}). Epoch referenced to the *B*-band maximum brightness.

Epoch	Ca II H&K	Si II 4130Å	Mg II	Fe II	S II W		Si II 5972Å	Si II 6355Å	Ca II trip
−9.6	–	–	–	–	–	–	–	13.6(0.1)	–
−8.5	–	11.8(1.2)	14.3(0.2)	18.9(0.2)	11.0(0.2)	11.3(0.1)	11.5(0.1)	13.0(0.1)	14.2(0.1)
−7.4	21.9(0.8)	11.0(0.2)	14.0(0.1)	18.7(0.1)	10.8(0.1)	11.1(0.1)	11.0(0.1)	12.7(0.1)	13.9(0.8)
−6.5	20.4(0.9)	10.7(0.3)	14.2(0.2)	18.8(0.1)	10.7(0.1)	10.7(0.1)	10.8(0.1)	12.5(0.1)	14.0(0.3)
−5.4	18.7(0.4)	10.5(0.7)	14.0(0.1)	18.4(0.1)	10.4(0.1)	10.6(0.1)	10.6(0.1)	12.2(0.1)	13.4(0.3)
−4.6	18.2(0.1)	10.1(0.4)	14.0(0.3)	18.1(0.1)	10.2(0.1)	10.2(0.1)	10.6(0.1)	12.1(0.1)	13.7(0.2)
+2.3	–	–	–	–	9.9(0.1)	9.5(0.1)	10.6(0.2)	11.5(0.1)	–
+3.3	16.3(0.6)	9.6(0.1)	11.8(0.1)	–	–	–	10.6(0.1)	11.4(0.1)	–
+4.2	15.3(0.2)	9.4(0.1)	10.6(0.1)	–	–	–	10.7(0.2)	11.2(0.1)	–
+10.5	–	–	–	–	9.0(0.1)	9.1(0.1)	12.1(0.1)	11.0(0.1)	11.9(0.1)
+12.4	–	–	–	10.0(0.1)	8.3(0.2)	8.7(0.2)	12.2(0.1)	10.8(0.1)	–
+17.4	–	–	–	–	–	–	–	10.5(0.1)	12.0(0.1)
+18.3	–	–	–	–	–	–	–	10.3(0.1)	12.0(0.1)
+19.5	–	–	–	–	–	–	–	10.3(0.1)	12.0(0.1)
+22.5	–	–	–	–	–	–	–	10.2(0.2)	12.0(0.1)
+24.5	–	–	–	–	–	–	–	10.1(0.2)	12.1(0.1)
+33.4	–	–	–	–	–	–	–	10.2(0.2)	12.1(0.1)
+34.4	–	–	–	–	–	–	–	10.5(0.3)	12.0(0.1)
+39.1	–	–	–	3.6(0.1)	–	–	–	10.4(0.3)	11.8(0.1)
+44.4	–	–	–	4.5(1.2)	–	–	–	10.9(0.3)	12.0(0.1)
+66.2	–	–	–	–	–	–	–	9.9(0.6)	12.2(0.1)
+96.2	–	–	–	–	–	–	–	7.8(0.5)	12.0(0.1)
+97.2	10.0(0.1)	–	2.7(0.2)	6.1(0.7)	–	–	–	8.1(0.3)	–
+99.1	10.3(0.3)	–	2.7(0.6)	5.8(0.2)	–	–	–	–	–
+137.2	9.9(0.5)	–	0.9(0.8)	–	–	–	–	7.6(1.1)	11.9(0.1)
+157.2	–	–	–	–	–	–	–	8.2(1.6)	12.1(0.2)
+212.5	–	–	–	–	–	–	–	7.3(1.9)	11.5(0.6)

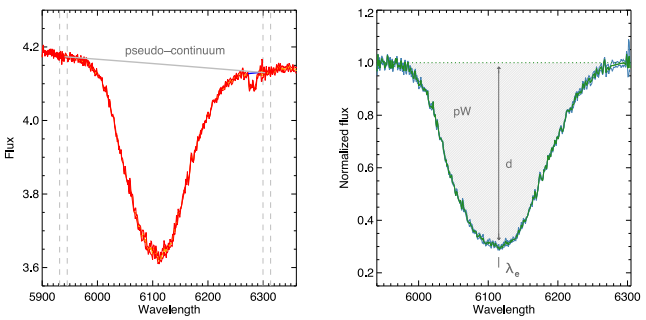

Figure 4. Description of the parameters measured in the spectra presented in this work. After determining the pseudo-continuum of the feature (as described in the text) the minimum of the feature (λ_e), its depth (d), and the pseudo-equivalent width (pW) are measured. From λ_e and using equation (1), the expansion velocity is calculated.

high R(Si II) values right after explosion and which decreases monotonically to R(Si II) $\lesssim 0.2$ around the epoch of maximum brightness; and (ii) low-Velocity Gradient (LVG) SN Ia show either no evolution or increasing R(Si II) values from explosion up to the peak brightness, when they tend to have higher R(Si II) values than HVG SN Ia. Additionally, by using a cluster analysis with other photometric and spectral properties, they defined a third group of underluminous SN Ia (FAINT) which actually have R(Si II) > 0.4 at the epoch of maximum brightness. This separation was even clearer when comparing the Si II λ6355 velocity gradient ($\dot{v}_{10}$, from the epoch of maximum brightness up to 10 d post-maximum) with the Δm_{15} decline rate parameter. While FAINT SN Ia show higher Δm_{15} values than the other two groups, LVG and HVG are disentangled by their velocity gradient ($\langle\dot{v}_{10}\rangle_{\rm HVG} = 97 \pm 16$, and $\langle\dot{v}_{10}\rangle_{\rm LVG} = 37 \pm 18$ km s^{-1} d^{-1} in the original BE05 sample).

Finally, this separation was also interpreted as differences in the mechanism responsible for the explosion (while HVG SN Ia could be produced by delayed-detonations, LVG SN would be the result of deflagrations), different heavy element mixing in the structure of the WD (more efficient for HVG SN Ia, and less in LVG SN Ia), or differences in the viewing angle assuming asymmetric explosions (two SNe Ia that are physically identical in three dimensions could be classified differently just because they are seen from different directions; Maeda et al. 2010). There is a remarkable continuity in the R(Si II) parameter at maximum light, enabling the presence of extreme, peculiar, and intermediate class objects.

BR06 proposed a different classification by constructing a diagram from the pseudo-equivalent widths (pWs) of the same Si II features used by Nugent et al. (1995) measured at maximum light. Although the spectral features used in BE05 and BR06 diagrams are the same, the depth of the feature used in the BE05 and the shape, width, and strength with respect the adjacent continuum used in the BR06 are not showing exactly the same information. Based on the position of the SN Ia in that diagram and on the actual appearance of the Si II λ6355 feature, BR06 distinguished four different groups: (i) shallow-silicon SN Ia (SS) show small pW values in the two features ($\lesssim$70 Å for Si II λ6355 and $\lesssim$25 Å for Si II λ5972); (ii) core-normal SN Ia (CN) have similar pW and shape of the λ6355 absorption, and higher pW Si II λ5972 values than shallow-silicon SN Ia (up to 105 Å). Differences were due to lower temperatures than the former; (iii) broad-line SN Ia (BL) have even higher Si II λ6355 pW values ($\gtrsim$105 Å), and show broader and deeper absorptions than those of the CN SN Ia; and (iv) Cool SN Ia (CL), which have higher pW for both features, specially

Table 3. Measured pseudo-equivalent widths (in Å). Epoch referenced to the *B*-band maximum brightness.

Epoch	Ca II H&K	Si II 4130Å	Mg II	Fe II	S II W	Si II 5972Å	Si II 6355Å	Ca II trip
−9.6	–	–	–	–	–	–	–	–
−8.5	–	15.6(3.1)	111.7(6.2)	139.8(6.7)	59.4(4.5)	19.3(1.5)	115.2(2.9)	242.2(2.7)
−7.4	–	13.9(1.5)	102.3(1.2)	136.0(1.6)	61.7(2.8)	16.8(1.2)	111.6(2.4)	221.7(4.2)
−6.5	242.8(5.8)	13.3(2.6)	107.3(3.6)	147.3(3.5)	66.1(3.8)	17.2(1.3)	112.6(3.1)	198.9(2.8)
−5.4	–	15.2(6.7)	113.5(4.5)	153.2(3.4)	71.0(3.2)	17.5(1.1)	113.0(4.6)	175.6(3.3)
−4.6	195.9(8.0)	15.5(3.4)	105.3(4.9)	149.5(5.5)	72.1(3.8)	15.9(1.9)	112.0(2.3)	169.9(3.4)
+2.3	–	–	–	–	80.3(3.5)	17.6(2.6)	111.2(3.7)	–
+3.3	122.3(6.0)	19.4(1.0)	103.4(1.9)	–	–	–	117.8(3.8)	–
+4.2	123.0(3.2)	21.5(1.4)	104.3(2.9)	–	–	17.2(1.6)	118.3(4.6)	–
+10.5	–	–	–	–	19.6(1.5)	45.0(2.7)	126.6(3.0)	284.8(2.9)
+12.4	–	–	–	284.2(7.6)	5.4(3.1)	79.1(3.1)	133.6(2.3)	–
+17.4	–	–	–	–	–	–	168.6(5.3)	309.8(2.6)
+18.3	–	–	–	–	–	–	181.1(5.5)	318.0(2.4)
+19.5	–	–	–	–	–	–	187.9(6.3)	330.1(2.4)
+22.5	–	–	–	–	–	–	203.2(6.6)	355.8(1.7)
+24.5	–	–	–	–	–	–	216.1(5.8)	393.2(4.8)
+33.4	–	–	–	–	–	–	254.2(5.9)	447.7(3.3)
+34.4	–	–	–	–	–	–	257.2(5.9)	439.2(5.6)
+39.1	–	–	–	437.6(11.9)	–	–	255.1(5.3)	463.4(3.5)
+44.4	–	–	–	422.4(4.7)	–	–	251.7(5.8)	480.6(4.2)
+66.2	–	–	–	–	–	–	245.8(8.9)	525.4(5.0)
+96.2	–	–	–	–	–	–	240.0(9.1)	553.8(6.2)
+97.2	137.6(9.4)	–	289.2(10.3)	252.0(8.4)	–	–	245.8(3.9)	–
+99.1	165.1(16.0)	–	317.3(12.2)	282.7(7.2)	–	–	–	–
+137.2	152.3(7.0)	–	279.3(5.8)	–	–	–	254.0(5.2)	494.9(4.7)
+157.2	–	–	–	–	–	–	254.6(6.2)	453.6(10.5)
+212.5	–	–	–	–	–	–	271.0(8.2)	412.5(34.8)

higher Si II λ5972 *pW* compared to the other groups ($\gtrsim$30 Å). As in the BE05 diagram, the intermediate regions between groups are populated with intermediate objects, showing a sequential continuity in the spectral properties for SN Ia.

There is a clear correspondence between both diagrams detailed above (see e.g. Parrent et al. 2014). BR06 CL SN Ia correspond to the BE05 FAINT SN Ia, which is to be expected, since both temperature and luminosity are controlled mainly by the ^{56}Ni mass. BR06 BL SN Ia correspond to the BE05 HVG SN Ia. This also makes sense, because broad Si II λ6355 absorption requires high Si II optical depth over a substantial velocity range, which makes it possible for the absorption minimum to shift appreciably with time. BL SN Ia may have thicker silicon layers than the CN SN Ia. Both BR06 CN and SS SN Ia correspond to the BE05 LVG SN Ia. The lower velocity range over which Si II has a high optical depth permits only a smaller shift in the absorption minimum with time.

Lately, WA09 proposed a different diagram between the *pW* of the Si II λ6355 absorption and the velocity of the same feature near *B*-band maximum light, instead of the *pW* Si II λ5972 absorption used in BR06 diagram. They distinguished between NORMAL SN Ia and HV, which showed a linear trend in the direction of higher velocity for higher *pW*, and also defined two other groups: underluminous SN Ia (which corresponds to 91bg-like SN Ia) with lower *pW* and lower velocities at maximum, and overluminous SN Ia (corresponding to 91T-like SN Ia) with lower velocities but similar *pW* than NORMAL SN Ia. This description has one-to-one correspondence with the BR06 groups.

This scheme summarizes the spectroscopic diversity discovered so far: a decreasing temperature sequence from 1991T-like (SS) to normal (CN) and 1991bg-like SN Ia (CL), plus the HV SN (BL) as a branch from the normal SN Ia group.

4 RESULTS AND DISCUSSION

4.1 SN 2014J in BE05, BR06 and WA09 diagrams

In Fig. 5, we show the two diagnostic diagrams by BE05 and BR06. In this and in the following figures, SN 2011fe has also been shown as a reference for comparisons. It is also a nearby object which shows few signs of extinction [$E(B-V) \sim 0.03$, accounting for both MW and host galaxy reddening; Mazzali et al. 2014. Spectra has been downloaded from WISeREP and the same spectral parameters have been measured in an homogeneous way for this work.[4]

The BE05 diagram has been filled with the original objects from BE05 and Altavilla et al. (2009). HVG SN Ia (in purple) show higher values of R(Si II) in the pre-maximum spectra which decrease near maximum light, while for LVG SN Ia the R(Si II) parameter evolves increasing monotonically or show no evolution at all. Compared to Si II λ6355, the Si II λ5972 absorption is produced by a transition with a higher excitation energy, so R(Si II) should increase in strength for higher temperatures (Nugent et al. 1995). This has been interpreted by BE05 as HVG SN having cooler temperatures at the line-forming regions that increase approaching maximum, while LVG SN, on the other hand, have high temperatures already well before maximum. Nugent et al. (1995) suggested the reason: at lower temperatures, the blanketing from Fe II and Co II increase the apparent strength of Si II λ5972, at higher temperatures Fe III and Co III wash out the feature. Moreover, Nugent et al. (1995) showed

[4] Although, as stated in the text, SN 2011fe spectra have been download from WISeREP, the actual sources that published the data used in this paper are Parrent et al. (2012), Pereira et al. (2013), Mazzali et al. (2014), and Maguire et al. (2014).

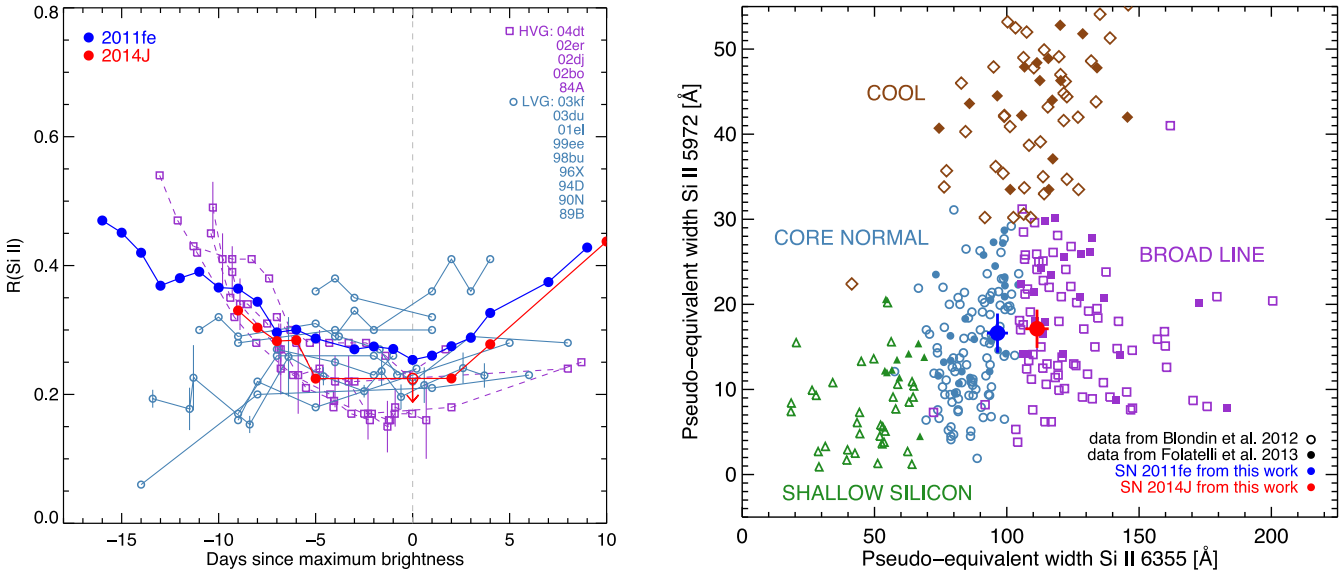

Figure 5. Left: diagram from BE05 where the evolution of the R(Si II) parameter is compared for HVG (blue) and LVG (purple) SN groups. Original data from Altavilla et al. (2009) are shown, and SN 2011fe and SN 2014J are overplotted. Right: diagram from BR06 where the pseudo-equivalent widths of the two Si II features at 5972 and 6355 are compared. Data from the Center for Astrophysics Supernova Program (CfA; Blondin et al. 2012, open symbols) and from the Carnegie Supernova Project (CSP; Folatelli et al. 2013, filled symbols) populate the diagram, and our measurements situate SN 2011fe (blue) and SN 2014J (red) on top.

Table 4. R(Si II) evolution for both SNe 2011fe and 2014J.

Epoch	2011fe	2014J
−16	0.47	–
−15	0.45	–
−14	0.42	–
−13	0.37	–
−12	0.38	–
−11	0.39	–
−10	0.37	–
−9	0.36	0.33
−8	0.34	0.30
−7	0.30	0.28
−6	0.30	0.28
−5	0.29	0.22
−3	0.27	–
−2	0.27	–
−1	0.27	–
0	0.25	–
1	0.26	–
2	0.27	0.22
3	0.29	–
4	0.33	0.28
7	0.37	–
9	0.43	–
10	–	0.44
12	–	0.72

a correlation between R(Si II) at maximum and the peak absolute magnitude, in the direction of brighter SN having lower R(Si II) values.

R(Si II) measurements for both SN 2014J and SN 2011fe are listed in Table 4. SN 2011fe has R(Si II) values higher than SN 2014J during the whole period shown in the left-hand panel of Fig. 5. In the pre-maximum phase, this can be interpreted as SN 2011fe having lower photospheric temperature due to more line blanketing by Fe and Co, and in the near maximum phase peaking at fainter absolute magnitude. Although the reported values in the literature point to similar or even slightly brighter M_B for SN 2011fe than for SN 2014J (14J: -19.26 ± 0.26 mag, Kawabata et al. 2014; -19.19 ± 0.10, Marion et al. 2015; 11fe: -19.45 ± 0.08, Tammann & Reindl 2011; -19.21 ± 0.15, Richmond & Smith 2012), the Δm_{15} values for SN 2011fe reported are slightly higher than for 2014J.

According to the relation between the B-band peak absolute magnitude and the Δm_{15}(B) parameter, which accounts for the brightness decline in the B band fifteen days after maximum (Phillips 1993; Phillips et al. 1999), these two SN lay perfectly on top of the bulk relation of normal SN Ia, well far from the subluminous SN Ia-91bg, and the overluminous super-*Chandra* SN Ia, as shown in Fig. 6. This supports the classification of SN 2014J as a normal SN Ia from a photometric point of view, allowing its use for cosmological analyses.

Due to the lack of very early R(Si II) measurements for SN 2014J, no definitive classification can be done using BE05 diagram, although it seems to tentatively follow other LVG SN Ia behaviour, and definitely have lower R(Si II) value at maximum than SN 2011fe. However, the near maximum light pW measurements allowed us to position 2014J in the BR06 diagram (see right-hand panel in Fig. 5). The BR06 diagram has been populated with data from the Center for Astrophysics Supernova Program (CfA; Blondin et al. 2012) and from the CSP (Folatelli et al. 2013) to define the regions covered by each of the four groups. Although SN 2011fe falls within the CN sector (corresponding to LVG in BE05 diagram) and SN 2014J are within the BL region (which corresponds to HVG in BE05), both are located close to the border defined between the two groups. The resulting BR06 classification is in agreement with what we found in BE05: while both objects tend to follow the behaviours of their corresponding groups, they both seem to be extreme objects of their classes and similar to each other.

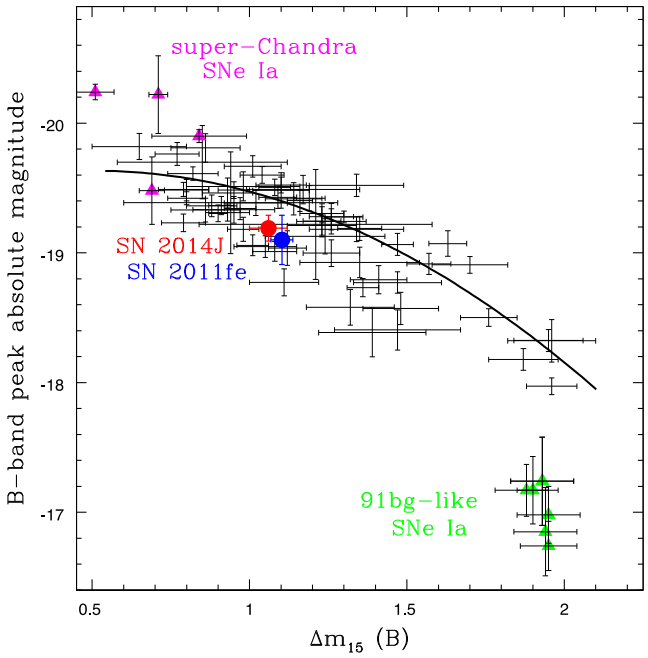

Figure 6. Relation between the *B*-band peak absolute magnitude and brightness decline in the *B* band 15 days after maximum [Δm_{15}(B); Phillips 1993; Phillips et al. 1999. The solid line represents the Phillips relation, that is followed by all normal SN Ia. Both SN 2011fe and SN 2014J are located on the bulk of normal objects. Although low-luminosity events (91bg-like) are well below the relation, the overluminous SN Ia (super-*Chandra*) may tentatively follow the solid line.

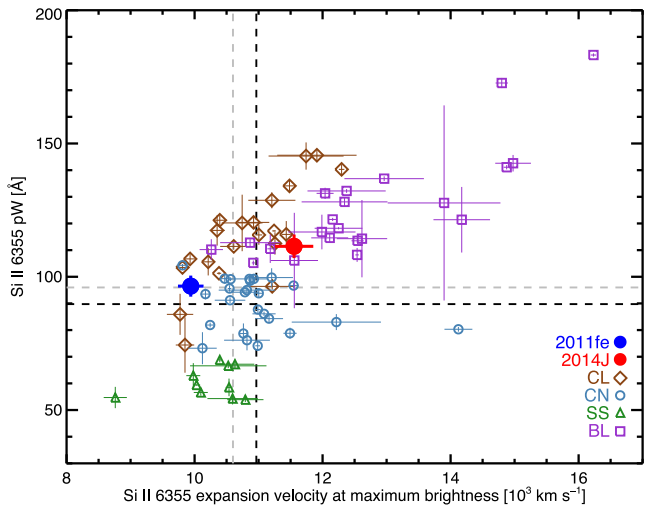

Figure 7. Diagram from WA09 comparing the pseudo-equivalent width of the Si II λ6355 feature at *B*-band maximum light with the velocity of the same feature at the same epoch. The diagram is populated with the SN Ia of the CSP taken from Folatelli et al. 2013. SN 2011fe are located closer to the 'normal' SN Ia group, while SN 2014J is in between the 'HV' and the 'normal' groups. Horizontal and vertical grey lines represent the average *pW* and *v* of the 'normal' group reported in WA09, and the black lines the average values for the CSP sample.

As a cross-check for the classification provided by these diagrams, in Fig. 7, we show the corresponding diagram presented by WA09. Since SN 2014J also shows higher velocities than SN 2011fe, it is also positioned within the BL group, but in the border with the CN region.

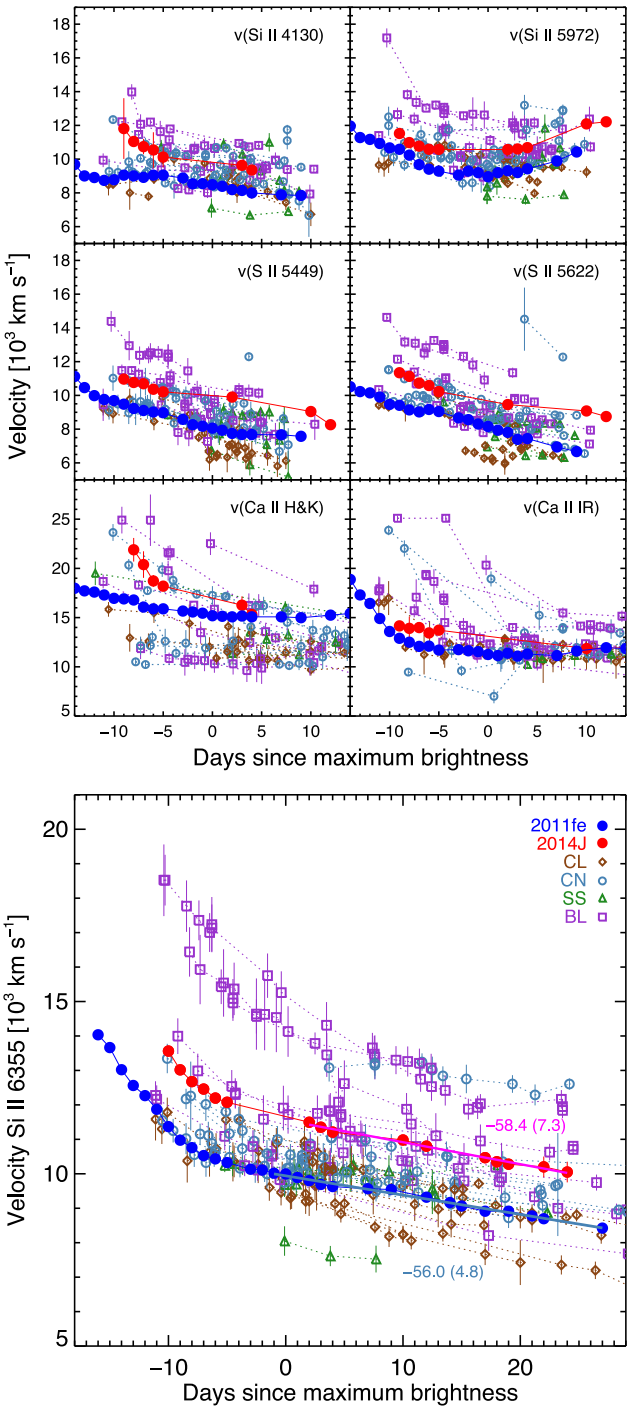

Figure 8. Velocity evolution of the main features in SN Ia spectra. Si II, S II, and Ca pairs are compared on top, and below the Si II λ6355 absorption velocity evolution are presented. SN 2011fe (in blue) and SN 2014J (in red) are shown on top of the CSP sample. In the bottom panel, two linear fits have performed to measure $\dot{v}_{10}$ for both SN 2011fe and 2014J.

4.2 Velocity and *pW* evolution

Fig. 8 shows the evolution of the expansion velocities of Si II, S II and Ca II features. In the background, we plotted in each panel the evolution of the velocities of the CSP SN Ia presented in Folatelli et al. (2013) coloured by the spectroscopic group defined in BR06 diagram. The overall expansion velocities of all features are higher for SN 2014J with respect to SN 2011fe. We note that in all panels,

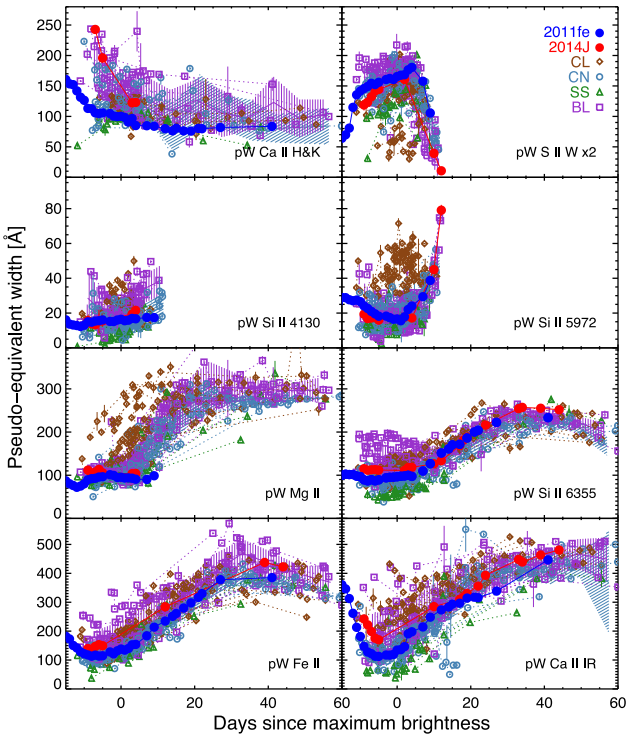

Figure 9. Pseudo-equivalent width evolution of the SN 2014J (in red) and SN 2011fe (in blue). The evolution of the pW in each feature for the four groups defined by BR06 obtained by measuring the pW from the CSP SN Ia sample are also shown as a reference. The shaded bands show the average and 1σ dispersion of CN and BL SN Ia.

while SN 2011fe is on top of other CN SN Ia velocity evolution, SN 2014J is on the bottom end of the BL group, which stresses it being a BL SN, but very close to the CN group, and is in agreement to what we found in the spectroscopic diagrams. For the Si II λ6355 absorption, we calculated the $\dot{v}_{10}$ for both SN. SN 2014J shows a velocity gradient of -58.4 ± 7.3 km s^{-1} d^{-1}, and for SN 2011fe we found -56.0 ± 4.8 km s^{-1} d^{-1}, in agreement with Pereira et al. (2013) who found -59.6 ± 3.2 km s^{-1} d^{-1}. Although SN 2014J's $\dot{v}_{10}$ is faster than the value found for SN 2011fe, both values are within the quoted errors.

Fig. 9 shows the evolution of the pWs of the eight strongest features measured in this work. The average evolution (and the 1σ deviation) of the pW in each feature for the four groups defined by BR06 obtained by measuring the pW from the CSP SN Ia sample are also shown for reference. In all panels, the BL and CN strips are mostly overlapping, making difficult any association of the studied objects to any of these groups. The differences are clearer in the evolution of the SS and CL groups. CL SN Ia show higher pW Mg II, and pW Si II λ5972, and lower pW S II W values, while SS have lower pW in all features except in the S II W absorption.

SN 2014J seems to be more associated with the BL class if one accounts for the behaviour of the Ca II H&K pW. The early higher values are characteristic of this group compared to the lower values that both the CN group and SN 2011fe show. This is confirmed by the lower pW values found post-maximum for SN 2014J and the BL group in the S II W feature, and the slightly higher pW values for the Si II λ4130, Si II λ5972, Fe II, and Ca II IR features. For Mg II, we only were able to measure the pW up to $\sim$10 d past-maximum light, and no conclusions can be made from this early phase. Finally, the Si II λ6355 pW evolution of both SN 2011fe and SN 2014J is very similar, although the value at maximum light is higher for 14J than for 11fe. In general, BL covers the SN 2014J evolution, and SN 2011fe pWs evolution follow the CN strip. However, they both are very similar, which underlines the proximity of the two objects within the two groups.

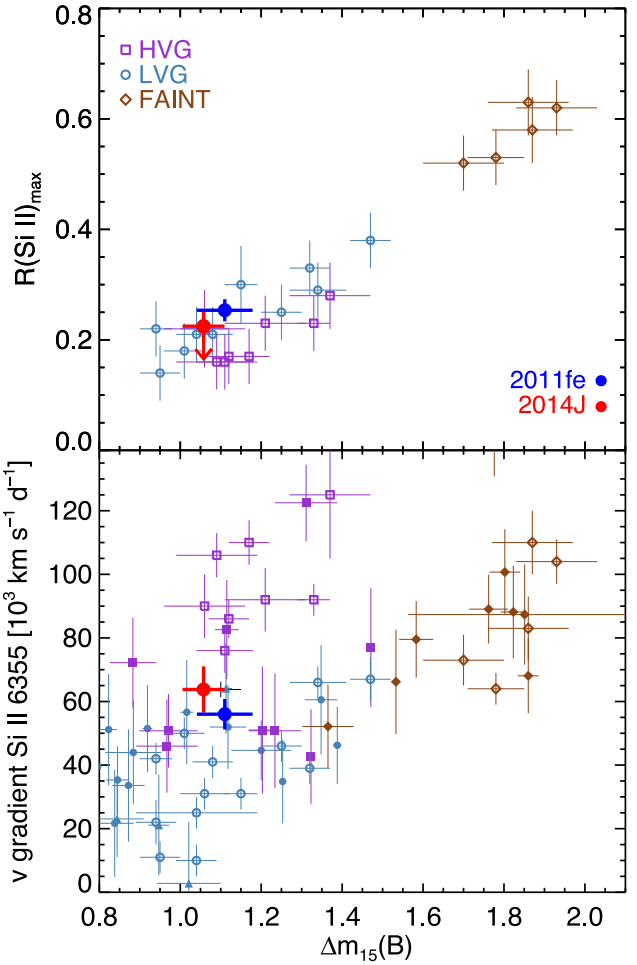

Figure 10. R(Si II) and v(Si II 6355) versus Δm_{15}(B) diagram. Data from Altavilla et al. (2009) and Benetti et al. (2005) are shown with unfilled symbols, and data from the CSP with filled symbols. SN 2014J (in red) and SN 2011fe (in blue) are situated showing that both are intermediate objects between LVG and HVG groups.

4.3 Spectral properties versus Δm_{15}(B)

Fig. 10 in its top panel shows the existing correlation between R(Si II) and Δm_{15}(B). Since R(Si II) traces the temperature, and Δm_{15} the brightness, the scatter the LVG objects introduces in the tight correlation between HVG and FAINT groups, can be interpreted as a need for a different physical parameter besides temperature to explain the heterogeneity of SN Ia, as discussed in BE05. Both SN 2011fe and 2014J follow the linear trend and, in this diagram SN 2014J is closer to the LVG SN Ia behaviour.

We showed in Fig. 8 that both SN Ia have similar velocity gradients. Their Δm_{15} (1.06 ± 0.06 for 2014J, averaging the values reported by Ashall et al. 2014; Tsvetkov et al. 2014; Kawabata et al. 2014; Marion et al. 2015, and 1.11 ± 0.07 for SN 2011fe, from Tammann & Reindl 2011; Richmond & Smith 2012; McClelland et al. 2013; Pereira et al. 2013) are similar as well, so in the

bottom panel of Fig. 10, they are positioned in the overlapping region between the LVG and the HVG groups. Here we include both the BE05 objects and CSP objects. They seem to agree well with the regions defined by their classifications. FAINT SN Ia have large Δm_{15} and $\dot{v}$ values, while the other two groups have lower Δm_{15} and are separated by their $\dot{v}$. Here, the expansion velocity gradient, $\dot{v}$, seems to be weakly correlated with Δm_{15}(B) for LVG and FAINT groups, while HVG SN Ia are separate from LVG by their larger $\dot{v}$ values.

In all diagnostics, SN 2014J follows the characteristics of BL/HVG SN Ia, being near the boundaries between CN/LVG subclasses. SN 2011fe is in the opposite situation falling in the CN/LVG regions in all parameter spaces, but close to the BL/HVG sector. Looking at most of the parameters studied in this work, the differences between SN 2011fe and 2014J are within the reported uncertainties. The subclasses in all diagnostics are not distinct in the sense that they are not separated by regions. However, SN Ia appear to be better described as a continuum than distinct subclasses, and SN 2011fe and 2014J being that close in the border of their subclasses is further evidence that the subclassifications are artificial.

5 CONCLUSIONS

We present the compilation of 27 spectra observed between 2014 January 22 and September 1 with the 2.5 m INT and 4.2 m WHT, located at the El Roque de Los Muchachos Observatory, La Palma. Observations were taken with different instruments and technical configurations. These and the reduction from the raw data are also described.

We measured several spectral parameters, including velocities, pWs, and absorption depths, for the most prominent features, and studied their evolution with time. With this information, and using SN 2011fe for comparison, we discussed the position of SN 2014J in BE05, BR06, and WA09 diagrams showing that SN 2014J is an intermediate object between the CN and BL SN Ia (according to BR06), also intermediate between the HVG and LVG groups (according to BE05), and in between the normal and HV groups (according to WA09). The most noticeable difference between the two objects is the difference of 1,500 km s^{-1} in their Si II 6355 expansion velocities around maximum light, as seen in the WA09 diagram. These diagnostic diagrams give more information about the state of the ejecta than the possible explosion mechanisms progenitor scenarios. In that sense, the proposed subclasses are better described by a continuous sequence than distinct groups, and this is supported by the existence of transitional SN Ia as SN 2011fe and SN 2014J. These findings support the classification of this middle-class SN 2014J as a standard event (Churazov et al. 2015) very similar to the bulk of SN Ia useful for measuring cosmological distances.

ACKNOWLEDGEMENTS

The authors gratefully acknowledge the anonymous referee for providing constructive comments and providing directions for additional work. Based on service observations (programme SW2014a08) made with the WHT, and on discretionary and Spanish CAT service observations made with the INT, both operated on the island of La Palma by the ING in the Spanish Observatorio del Roque de los Muchachos of the Instituto de Astrofísica de Canarias. We thank the ING Director for having made public the INT data as soon as they were obtained. We also acknowledge the observers who kindly donated their time to monitor SN2014J on both the WHT and the INT. We acknowledge Giuseppe Altavilla, Stefano Benetti for providing the data used in the left-hand panel of Fig. 5 and Gastón Folatelli for the CSP data for Figs 5, 7, 8, 9 and 10. Support for LG and MH is provided by the Ministry of Economy, Development, and Tourism's Millennium Science Initiative through grant IC120009, awarded to The Millennium Institute of Astrophysics, MAS. LG acknowledges support by CONICYT through FONDECYT grant 3140566. Support for MEMR and MM is provided by DGICYT grant AYA2010-21887-C04-02. This work is partially funded by DGICYT grant AYA2013-47742-C4-4-P. JIG-H, HL and JAR-M acknowledge financial support from the Spanish Ministry of Economy and Competitiveness (MINECO) under the 2011 Severo Ochoa programme MINECO SEV-2011-0187 JIG-H also acknowledge the 2013 Ramón y Cajal programme MINECO RYC-2013-14875, and the Spanish ministry project MINECO AYA2014-56359-P. EAC acknowledges the support of the STFC.

REFERENCES

Altavilla G. et al., 2009, ApJ, 695, 135
Amanullah R. et al., 2014, ApJ, 788, L21
Ashall C., Mazzali P., Bersier D., Hachinger S., Phillips M., Percival S., James P., Maguire K., 2014, MNRAS, 445, 4427
Benetti S. et al., 2005, ApJ, 623, 1011 (BE05)
Betoule M. et al., 2014, A&A, 568, A22
Blondin S. et al., 2012, AJ, 143, 126
Bonev T. et al., 2014, Astronomer's Telegram, 5829, 1
Branch D. et al., 2006, PASP, 118, 560 (BR06)
Branch D. et al., 2007, PASP, 119, 709
Brown P. J. et al., 2015, ApJ, 805, 74
Cao Y., Kasliwal M. M., McKay A., Bradley A., 2014, Astronomer's Telegram, 5786, 1
Chandler C. J., Marvil J., 2014, Astronomer's Telegram, 5812, 1
Chandra P., Basu A., Ray A., Chakraborty S., 2014, Astronomer's Telegram, 5804, 1
Chomiuk L. et al., 2015, preprint (arXiv:1510.07662)
Churazov E. et al., 2014, Nature, 512, 406
Churazov E. et al., 2015, ApJ, 812, 62
Conley A. et al., 2008, ApJ, 681, 482
Crotts A. P. S., 2015, ApJ, 804, L37
Dalcanton J. J. et al., 2009, ApJS, 183, 67
Denisenko D. et al., 2014, Astronomer's Telegram, 5795, 1
Diehl R., 2015, Astron. Nachr., 336, 464
Diehl R. et al., 2014, Science, 345, 1162
Fitzpatrick E. L., 1999, PASP, 111, 63
Folatelli G. et al., 2013, ApJ, 773, 53
Foley R. J. et al., 2014, MNRAS, 443, 2887
Fossey S. J., Cooke B., Pollack G., Wilde M., Wright T., 2014, Cent. Bur. Electron. Telegrams, 3792, 1
Friesen B., Baron E., Wisniewski J. P., Parrent J. T., Thomas R. C., Miller T. R., Marion G. H., 2014, ApJ, 792, 120
Gao J., Jiang B. W., Li A., Li J., Wang X., 2015, ApJ, 807, L26
Garavini G. et al., 2007, A&A, 470, 411
González-Hernández J. I., Génova-Santos R., Rubiño-Martin J. A., Ruiz-Lapuente P., 2014, Astronomer's Telegram, 5843, 1
Goobar A. et al., 2014, ApJ, 784, L12
Goobar A. et al., 2015, ApJ, 799, 106
Graham M. L. et al., 2015, ApJ, 801, 136
Guy J. et al., 2007, A&A, 466, 11
Hatano K., Branch D., Lentz E. J., Baron E., Filippenko A. V., Garnavich P. M., 2000, ApJ, 543, L49
Hillebrandt W., Kromer M., Röpke F. K., Ruiter A. J., 2013, Frontiers Phys., 8, 116
Hoyle F., Fowler W. A., 1960, ApJ, 132, 565
Iben I., Jr, Tutukov A. V., 1984, ApJS, 54, 335

Jha S., Riess A. G., Kirshner R. P., 2007, ApJ, 659, 122
Kawabata K. S. et al., 2014, ApJ, 795, L4
Kelly P. L. et al., 2014, ApJ, 790, 3
Kotak R., 2014, Astronomer's Telegram, 5816, 1
Kutsuna M., Shigeyama T., 2015, PASJ, 67, 54
Lampeitl H. et al., 2010, ApJ, 722, 566
Li W., Chornock R., Leaman J., Filippenko A. V., Poznanski D., Wang X., Ganeshalingam M., Mannucci F., 2011, MNRAS, 412, 1473
Livio M., Riess A. G., 2003, ApJ, 594, L93
Lundqvist P. et al., 2015, A&A, 577, A39
McClelland C. M., Garnavich P. M., Milne P. A., Shappee B. J., Pogge R. W., 2013, ApJ, 767, 119
Ma B., Wei P., Shang Z., Wang L., Wang X., 2014, Astronomer's Telegram, 5794, 1
Maeda K., Taubenberger S., Sollerman J., Mazzali P. A., Leloudas G., Nomoto K., Motohara K., 2010, ApJ, 708, 1703
Maguire K. et al., 2014, MNRAS, 444, 3258
Maoz D., Mannucci F., Nelemans G., 2014, ARA&A, 52, 107
Margutti R., Parrent J., Kamble A., Soderberg A. M., Foley R. J., Milisavljevic D., Drout M. R., Kirshner R., 2014, ApJ, 790, 52
Marion G. H. et al., 2015, ApJ, 798, 39
Massey P., Strobel K., Barnes J. V., Anderson E., 1988, ApJ, 328, 315
Mazzali P. A. et al., 2014, MNRAS, 439, 1959
Moreno-Raya M. E., Galbany L., Lopez-Sanchez A. R., Dominguez I., Vilchez J. M., Carnero A., Molla M., 2014, Astronomer's Telegram, 5827, 1
Moreno-Raya M. E. et al., 2015, preprint (arXiv:1510.07662)
Nielsen M. T. B., Gilfanov M., Bogdán Á., Woods T. E., Nelemans G., 2014, MNRAS, 442, 3400
Nordin J. et al., 2011, A&A, 526, A119
Nugent P., Phillips M., Baron E., Branch D., Hauschildt P., 1995, ApJ, 455, L147
Oke J. B., 1990, AJ, 99, 1621
Parrent J. T. et al., 2012, ApJ, 752, L26
Parrent J., Friesen B., Parthasarathy M., 2014, Ap&SS, 351, 1
Patat F. et al., 2015, A&A, 577, A53
Pereira R. et al., 2013, A&A, 554, A27
Pérez-Torres M. A. et al., 2014, ApJ, 792, 38
Phillips M. M., 1993, ApJ, 413, L105
Phillips M. M., Lira P., Suntzeff N. B., Schommer R. A., Hamuy M., Maza J., 1999, AJ, 118, 1766
Poppe B., Plaggenborg T., Zheng W., Shivvers I., Itagaki K., Filippenko A. V., Kunz J., 2015, J. Am. Assoc. Var. Star Obs., 43, 43
Richardson N., Artigau E., Laflamme D., Malenfant B., 2014, Astronomer's Telegram, 5840, 1
Richmond M. W., Smith H. A., 2012, J. Am. Assoc. Var. Star Obs., 40, 872
Ritchey A. M., Welty D. E., Dahlstrom J. A., York D. G., 2015, ApJ, 799, 197
Ruiz-Lapuente P., 2014, New Astron. Rev., 62, 15
Schlafly E. F., Finkbeiner D. P., 2011, ApJ, 737, 103
Siverd R. J., Goobar A., Stassun K. G., Pepper J., 2015, ApJ, 799, 105
Soker N., Kashi A., García-Berro E., Torres S., Camacho J., 2013, MNRAS, 431, 1541
Sokolovsky K. V. et al., 2014, Astronomer's Telegram, 6197, 1
Srivastav S., Ninan J. P., Anupama G. C., Sahu D. K., Ojha D. K., 2014, Astronomer's Telegram, 5876, 1
Stone R. P. S., 1977, ApJ, 218, 767
Sullivan M. et al., 2010, MNRAS, 406, 782
Tammann G. A., Reindl B., 2011, preprint (arXiv:1112.0439)
Telesco C. M. et al., 2015, ApJ, 798, 93
Tsvetkov D. Y., Metlov V. G., Shugarov S. Y., Tarasova T. N., Pavlyuk N. N., 2014, Contrib. Astron. Obs. Skalnate Pleso, 44, 67
Vacca W. D. et al., 2015, ApJ, 804, 66
Vallely P. et al., 2015, preprint (arXiv:1512.02608)
Wang X. et al., 2009, ApJ, 699, L139 (WA09)
Iben, Jr, I.Whelan J., 1973, ApJ, 186, 1007
Yaron O., Gal-Yam A., 2012, PASP, 124, 668
Zheng W. et al., 2014, ApJ, 783, L24

This paper has been typeset from a TEX/LATEX file prepared by the author.